Check for updates

Tailoring carrier dynamics in perovskite solar cells *via* precise dimension and architecture control and interfacial positioning of plasmonic nanoparticles†

Xun Cui,‡[ab] Yihuang Chen,‡[a] Meng Zhang,[a] Yeu Wei Harn,[a] Jiabin Qi,[a] Likun Gao,[a] Zhong Lin Wang,[a] Jinsong Huang,[c] Yingkui Yang [ID] *[b] and Zhiqun Lin [ID] *[a]

Placing plasmonic nanoparticles (NPs) in close proximity to semiconductor nanostructures renders effective tuning of the optoelectronic properties of semiconductors through the localized surface plasmon resonance (LSPR)-induced enhancement of light absorption and/or promotion of carrier transport. Herein, we report on, for the first time, the scrutiny of carrier dynamics of perovskite solar cells (PSCs) *via* sandwiching monodisperse plasmonic/dielectric core/shell NPs with systematically varied dielectric shell thickness yet fixed plasmonic core diameter within an electron transport layer (ETL). Specifically, a set of Au NPs with precisely controlled dimensions (*i.e.*, fixed Au core diameter and tunable SiO_2 shell thickness) and architectures (plain Au NPs and plasmonic/dielectric Au/SiO_2 core/shell NPs) are first crafted by capitalizing on the star-like block copolymer nanoreactor strategy. Subsequently, these monodisperse NPs are sandwiched between the two consecutive TiO_2 ETLs. Intriguingly, there exists a critical dielectric SiO_2 shell thickness, below which hot electrons from the Au core are readily injected to TiO_2 (*i.e.*, hot electron transfer (HET)); this promotes local electron mobility in the TiO_2 ETL, leading to improved charge transport and increased short-circuit current density (J_{sc}). It is also notable that the HET effect moves up the Fermi level of TiO_2, resulting in an enhanced built-in potential and open-circuit voltage (V_{oc}). Taken together, the PSCs constructed by employing a sandwich-like TiO_2/Au NPs/TiO_2 ETL exhibit both greatly enhanced J_{sc} and V_{oc}, delivering champion PCEs of 18.81% and 19.42% in planar and mesostructured PSCs, respectively. As such, the judicious positioning of rationally designed monodisperse plasmonic NPs in the ETL affords effective tailoring of carrier dynamics, thereby providing a unique platform for developing high-performance PSCs.

Broader context

Plasmonic nanoparticles (NPs) have been introduced into photovoltaic devices, aiming initially at increasing light absorption. In the case of perovskite solar cells (PSCs) incorporating plasmonic NPs, recent reports have shown the improvement of the photovoltaic performance; however, negligible light absorption enhancement was observed. In this context, investigaton into the mechanisms of plasmonic enhancement in PSCs is valuable and urgently needed. In addition, the dielectric SiO_2 shell thickness can significantly affect the electronic characteristics of Au/SiO_2 core/shell NPs. Clearly, the ability to systematically alter the SiO_2 shell thickness at the nanometer scale enables a tunable electronic characteristic of Au/SiO_2 core/shell NPs. However, while highly desirable, it is challenging to precisely and systematically control the dimensions and architecture of Au/SiO_2 core/shell NPs at the nanoscale. In this work, we develop a robust amphiphilic star-like block copolymer nanoreactor strategy to create a set of monodisperse plasmonic NPs of different sizes and architectures (*i.e.*, plain Au and Au/SiO_2 core/shell NPs), and subsequently scrutinize, for the first time, the effects of the dielectric SiO_2 shell thickness and the positioning of plasmonic NPs on the charge carrier dynamics and thus the performance of PSCs. This study offers insight into the tailoring of charge carrier dynamics in PSCs *via* rational design and placement of monodisperse plasmonic/dielectric NPs with tunable dielectric shell thickness to achieve high-performance PSCs.

[a] *School of Materials Science and Engineering, Georgia Institute of Technology, Atlanta, GA 30332, USA. E-mail: zhiqun.lin@mse.gatech.edu, ykyang@mail.scuec.edu.cn*

[b] *Key Laboratory of Catalysis and Energy Materials Chemistry of Ministry of Education & Hubei Key Laboratory of Catalysis and Materials Science, South-Central University for Nationalities, Wuhan 430074, China*

[c] *Department of Applied Physical Sciences, University of North Carolina, Chapel Hill, NC 27599, USA*

† Electronic supplementary information (ESI) available: Detailed description of the experimental methods and additional data and figures. See DOI: 10.1039/c9ee03937f

‡ Equal contribution.

This journal is © The Royal Society of Chemistry 2020

Energy Environ. Sci., 2020, **13**, 1743–1752 | **1743**

Introduction

Recent research has witnessed unprecedented advances in organolead halide perovskite solar cells (PSCs) with power conversion efficiency (PCE) leaping from approximately 3% to 25.2% comparable to that of silicon-based solar cells.[1–6] Various effective strategies have been developed for increasing the performance of PSCs, including perovskite absorber design and crystal growth,[7–10] defect passivation,[11] and interface engineering.[12,13] Among them, interface engineering stands out as an effective means of enabling control over carrier dynamics within the entire device. The implementation of plasmonic nanoparticles (NPs) in either the absorber or carrier transport layers of a solar cell represents a promising route to bettering the harvesting of incident light[14] *via* localized surface plasmon resonance (LSPR) effect[15–17] and engineering the carrier dynamics (*i.e.*, promoting carrier transport and collection)[18–20] *via* regulating their optical and electronic characteristics. In the particular case of PSCs incorporating plasmonic NPs, recent reports have indeed shown the improvements of the photovoltaic performance.[18–20] However, negligible light absorption enhancement was observed. In this context, performing fundamental research to gain deep insights into the plasmonic enhancement mechanisms is valuable and urgently needed. Notably, for the most commonly used TiO_2 electron transport layer (ETL) in PSCs, its trap states need to be filled up by photo-generated electrons under illumination to render TiO_2 with an improved photoconductivity.[21] Placing Au NPs in close contact with TiO_2 imparts hot electron transfer (HET) from Au NPs to occupy the trap states of TiO_2, leading to increased charge carrier density in TiO_2. Consequently, the charge mobility of TiO_2 increases, which facilitates the extraction of photo-generated electrons from the absorber at the TiO_2/absorber interface and their transport.

The strength of the LSPR effect of noble metal NPs (*e.g.*, Au and Ag) depends heavily on the NP size. For hot electrons, they are efficiently generated in noble metal nanostructures with a size less than 20 nm.[22] Another factor largely affecting the strength of the LSPR effect is the dielectric property of the surrounding medium. It has been reported that the dielectric SiO_2 shell of Au/SiO_2 core/shell NPs prohibits HET generated from Au from jumping over the Schottky barrier unless the SiO_2 thickness is less than its tunneling barrier height ($\sim$ 3 nm).[23] Clearly, the ability to systematically alter the SiO_2 shell thickness at the nanometer scale enables a tunable electronic characteristic of Au/SiO_2 core/shell NPs. This, however, has yet to be largely explored. In this context, despite recent advances in implementing the LSPR effect of plasmonic NPs in PSCs, our understanding on how the dielectric shell of varied thickness influences the HET of the plasmonic core and in turn the performance of the resulting PSCs remains comparatively elusive.

To date, it is still highly desirable but challenging to precisely and systematically control the dimensions and architecture of plasmonic NPs at the nanoscale. Herein, we develop a robust amphiphilic-*star*-like-*block*-copolymer nanoreactor strategy to create an array of monodisperse plasmonic NPs of different sizes and architectures (*i.e.*, plain Au and Au/SiO_2 core/shell NPs),

and subsequently scrutinize, for the first time, the effects of dielectric SiO_2 shell thickness and the positioning of plasmonic NPs (*i.e.*, sandwiched within TiO_2 ETL (scenario 1) and at the perovskite/TiO_2 ETL interface (scenario 2)) on the charge carrier dynamics and thus the performance of PSCs. First, two amphiphilic star-like block copolymers, namely, poly(acrylic acid)-*block*-polystyrene (denoted PAA-*b*-PS) and poly(4-vinyl pyridine)-*block*-poly(*t*-butyl acrylate)-*block*-poly(ethylene oxide) (denoted P4VP-*b*-P*t*BA-*b*-PEO), with well-defined molecular weight and low polydispersity index are synthesized *via* controlled living radical polymerization. They were then exploited as nanoreactors to craft uniform Au NPs and Au/SiO_2 core/shell NPs, respectively. It is important to note that Au and SiO_2 are template-grown by capitalizing on P4VP and PAA (hydrolyzed from P*t*BA) blocks, respectively. Thus, the Au core diameter and the SiO_2 shell thickness can be precisely controlled by tuning the molecular weight of the inner P4VP and intermediate P*t*BA blocks *via* controlling the atom transfer radical polymerization (ATRP) time of 4-vinyl pyridine (4VP) and *t*-butyl acrylate (*t*BA), respectively. As a result, a set of Au/SiO_2 NPs at a constant Au core diameter and different SiO_2 shell thickness are conveniently produced.

Undoubtedly, this effective and robust strategy ensures the subsequent scrutinization of the effects of dielectric SiO_2 shell thickness and the mechanism research. By incorporating plain Au NPs and Au/SiO_2 NPs of varied SiO_2 shell thickness (t_{SiO_2} = 2, 6 and 10 nm at fixed D_{Au} = 12 nm) in PSCs with two different positioning scenarios, that is, encapsulated inside the TiO_2 ETL and deposited at the perovskite/TiO_2 ETL interface, we uncover the mechanism with which the charge carrier dynamics of PSCs is affected. Intriguingly, rather than the optical effect of plasmonic NPs, their electronic characteristic was found to markedly improve the photovoltaic performance of PSCs, as substantiated by time-resolved photoluminescence spectroscopy (TRPL), intensity modulated photocurrent spectroscopy (IMPS), and intensity modulated photovoltage spectroscopy (IMVS) measurements. Investigation into the effect of the SiO_2 shell thickness reveals the existence of a critical dielectric SiO_2 shell thickness, below which HET from the Au core to TiO_2 ETL readily occurs, thereby improving electron mobility in the TiO_2 ETL due to the filled trap states in TiO_2 and resulting in improved charge transfer from perovskite to TiO_2 and transport within TiO_2 and thus increased short-circuit current density (J_{sc}). Concurrently, the carrier density in TiO_2 is improved due to the HET effect that moves up the Fermi level of TiO_2 and reduces its work function, giving rise to an enhanced open-circuit voltage (V_{oc}) as evidenced by Kelvin probe measurement and Mott–Schottky analysis. In sharp contrast, beyond the critical SiO_2 shell thickness (*i.e.*, 6 nm and 10 nm), only a slight increase of J_{sc} was observed due to the LSPR-induced charge separation/transfer as a result of the near electromagnetic field (NEF) enhancement effect within the TiO_2 ETL. The J_{sc} is yet much smaller than the device with the SiO_2 shell below the critical thickness. Moreover, owing to the absence of HET, no V_{oc} enhancement for plasmonic NPs with 6 nm and 10 nm SiO_2 shell-incorporated devices was seen.

The optimized planar and mesostructured PSCs based on a $FA_{0.85}MA_{0.15}PbI_{2.55}Br_{0.45}$ absorber assembled with a

1744 | *Energy Environ. Sci.*, 2020, **13**, 1743–1752

This journal is © The Royal Society of Chemistry 2020

sandwich-shaped ETL (*i.e.*, impregnating Au NPs within TiO$_2$ ETL) deliver champion PCEs of 18.81% and 19.42%, respectively. It is notable that the devices with the sandwiched placement of plasmonic NPs within the ETL (scenario 1) outperform those constructed by situating plasmonic NPs at the perovskite/TiO$_2$ interface (scenario 2). This is not surprising as plamonic NPs largely function as the recombination center for charge carriers, leading to decreased J_{sc} and V_{oc} and thus lowered PCEs. This study offers insight into the tailoring of charge carrier dynamics at the interface of PSCs *via* rational design and placement of monodisperse plasmonic/dielectric NPs of tunable dielectric shell thickness to achieve plasmonic enhancement-enabled high-performance PSCs.

Results and discussion

Synthesis and characterization of plain Au and Au/SiO$_2$ core/shell nanoparticles

Due to the branched yet compact architecture, amphiphilic star-like block copolymers with each block copolymer arm covalently connected to a central small molecular core form a unimolecular micelle in solution. Such unimolecular micellar architecture is static rather than dynamic as in conventional micelles produced from self-assembly of linear amphiphilic block copolymers in selective solvents. The conventional micelles may be readily disassembled upon the change of experimental conditions (*e.g.*, concentration, solvent, pH, temperature, *etc.*). Nonetheless, the structurally stable unimolecular micelles of an amphiphilic star-like block copolymer are then employed as a nanoreactor for crafting inorganic NPs. Fig. 1 depicts the synthetic routes to plain Au NPs and Au/SiO$_2$ core/shell NPs using the amphiphilic star-like PAA-*b*-PS diblock copolymers (central panel; first row) and P4VP-*b*-PtBA-*b*-PEO triblock copolymers (central panel; third row), respectively, as nanoreactors. Amphiphilic PAA-*b*-PS is synthesized *via* a sequential atom transfer radical polymerization (ATRP) of *t*-butyl acrylate (*t*BA) and styrene (St) from a β-cyclodextrin-based macroinitiator, followed by the hydrolysis of inner poly(*t*-butyl acrylate) (PtBA) blocks (Table S1, ESI†).[24,25] The coordination interaction between the carboxyl groups (–COOH) of PAA blocks and the metal moiety of Au precursors (HAuCl$_4$) preferentially partitions the precursors within the regime occupied by inner hydrophilic PAA blocks of the star-like PAA-*b*-PS diblock copolymer, leading to the formation of Au NPs intimately capped by outer PS blocks (*i.e.*, PS-capped Au NPs; left panel, first row). Similarly, amphiphilic P4VP-*b*-PtBA-*b*-PEO is prepared *via* a combination of sequential ATRP of 4-vinyl pyridine (4VP) and *t*BA from a β-cyclodextrin-based macroinitiator with a click reaction (Table S1, ESI†).[25,26] Likewise, the inner hydrophilic P4VP blocks and intermediate hydrophilic poly(acrylic acid) (PAA) blocks converted from the hydrolysis of hydrophobic PtBA render the formation of the Au core (from central to right panels; third row; Fig. 1) and SiO$_2$ shell (from right to left panels; fourth row; Fig. 1) through the strong coordination interactions between the precursors (HAuCl$_4$ for Au and tetra-ethoxysilane (TEOS) for SiO$_2$) and the functional groups in the
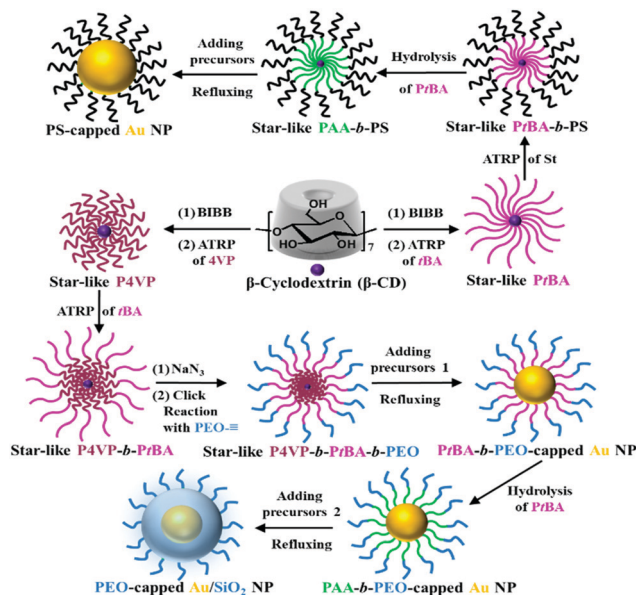

Fig. 1 Stepwise representation of the synthetic route to plain Au and Au/SiO$_2$ core/shell NPs by capitalizing on amphiphilic star-like poly(acrylic acid)-*block*-polystyrene (PAA-*b*-PS) diblock copolymer and poly(4-vinyl pyridine)-*block*-poly(*t*-butyl acrylate)-*block*-poly(ethylene oxide) (P4VP-*b*-PtBA-*b*-PEO) triblock copolymer, respectively, as nanoreactors.
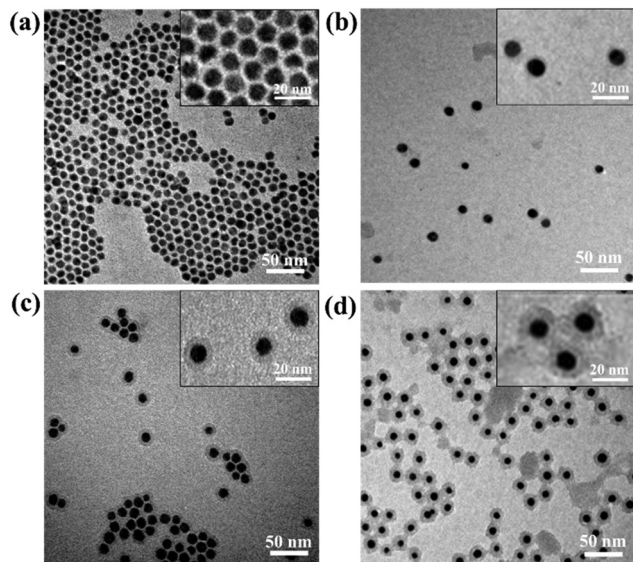
P4VP (pyridal groups) and PAA (–COOH groups) blocks, respectively. It is noteworthy that the Au core diameter and the SiO$_2$ shell thickness in PEO-capped Au/SiO$_2$ core/shell NPs can be precisely controlled by tailoring the molecular weights (*i.e.*, lengths) of the inner P4VP and intermediate PtBA blocks, respectively, *via* controlling the sequential ATRP time of 4VP and *t*BA due to the living radical polymerization characteristic of ATRP.[27]

As discussed above, hot electrons are effectively generated when the size of the plasmonic nanostructures is less than 20 nm.[22] Thus, in order to explore the shell thickness-dependent plasmonic effect of Au NPs and Au/SiO$_2$ NPs introduced in PSCs, the Au core diameter needs to be less than 20 nm and remain constant for comparison. Fig. 2 compares the TEM images of the as-synthesized plain PS-capped Au NPs (D_{Au} = 12 nm; Fig. 2a) and PEO-capped Au/SiO$_2$ core/shell NPs at a constant D_{Au} of 12 nm and judiciously varied SiO$_2$ shell thickness of 2, 6 and 10 nm (Fig. 2b–d). All NPs are highly uniform with narrow size distribution (Table S2, ESI†). Clearly, the nanoreactor strategy provides remarkable flexibility in synthesizing core/shell NPs with tailored shell thickness *via* controlling the molecular weight of the PtBA block solely during ATRP of *t*BA (Fig. 2b–d). The Au core appears darker and is surrounded by the lighter SiO$_2$ shell, as clearly evidenced by TEM imaging.

Impacts of interfacial positioning and dielectric SiO$_2$ shell thickness on device performance

The plain Au NPs and Au/SiO$_2$ core/shell NPs are then exploited to scrutinize the effects of dielectric SiO$_2$ shell thickness and the positioning of these plasmonic NPs on charge carrier dynamics in PSCs and the resulting device performance. First, we optimized the thickness of the TiO$_2$ ETL (see Fig. S1, S2a–d, Table S3, and
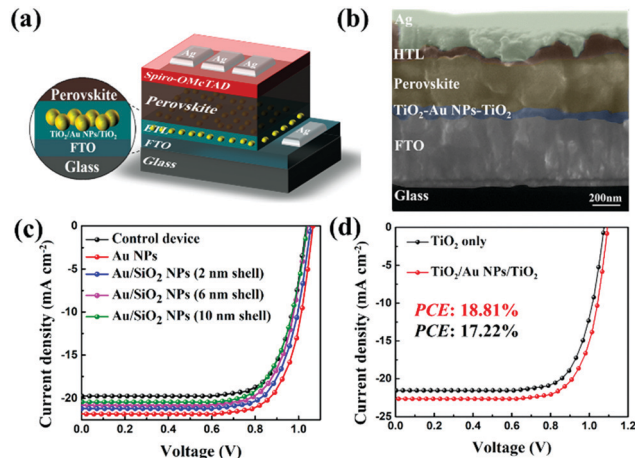
This journal is © The Royal Society of Chemistry 2020

Energy Environ. Sci., 2020, **13**, 1743–1752 | **1745**

Fig. 2 TEM images of plain Au and Au/SiO$_2$ core/shell NPs at a fixed Au core diameter and varied SiO$_2$ shell thickness. (a) Plain Au NPs with a diameter of 12 nm. (b–d) Au/SiO$_2$ core/shell NPs. The diameter of the Au core and thickness of the SiO$_2$ shell are as follows: (b) 12 nm Au and 2 nm SiO$_2$, (c) 12 nm Au and 6 nm SiO$_2$, and (d) 12 nm Au and 10 nm SiO$_2$, respectively. Insets show the close-ups of NPs.

Fig. 3 (a) Schematic of the planar PSC (denoted p-PSC) assembled by capitalizing on plain Au NPs sandwiched between a double-layer TiO$_2$ ETL. (b) Cross sectional SEM image of the p-PSC fabricated on a sandwiched TiO$_2$ ETL (*i.e.*, scenario 1: TiO$_2$/Au NPs/TiO$_2$ ETL). (c) J–V characteristics of perovskite CH$_3$NH$_3$PbI$_3$ solar cells constructed with TiO$_2$ only (control device) and with Au NPs and Au/SiO$_2$ NPs sandwiched between double-layer TiO$_2$ as ETLs. (d) J–V characteristics of perovskite FA$_{0.85}$MA$_{0.15}$PbI$_{2.55}$Br$_{0.45}$ solar cells with (PCE = 18.81%) and without Au NPs (PCE = 17.22%) sandwiched between the double-layer TiO$_2$ ETL.

Note S1, ESI,† for detailed optimization process) and found that a double-layered TiO$_2$ film as the ETL favors an optimum device performance. We note that all polymer ligands (PS as in PS-capped Au NPs, and PEO as in PEO-capped Au/SiO$_2$ core/shell NPs) are removed during the sintering treatment of the TiO$_2$ ETL. Appropriate positioning of plasmonic NPs can effectively improve the photovoltaic performance of PSCs. In our study, two different assembly scenarios for incorporating plasmonic NPs into PSCs are invoked, that is, either sandwiched within the TiO$_2$ ETL (scenario 1, Fig. 3a) or incorporated at the perovskite CH$_3$NH$_3$PbI$_3$/TiO$_2$ ETL interface (scenario 2, Fig. S3, ESI†).

As the first attempt, the plasmonic NPs (*i.e.*, plain Au NPs and Au/SiO$_2$ core/shell NPs) are deposited at the CH$_3$NH$_3$PbI$_3$/TiO$_2$ interface (scenario 2) *via* spin-coating. It was found that the direct contact between the Au NPs and perovskite CH$_3$NH$_3$PbI$_3$ absorber deteriorates the device performance as the Au NPs act as the recombination centers for photo-generated charge carriers in the perovskite film as reported in the literature.[20] In scenario 2, devices fabricated with either plain Au NPs or Au/SiO$_2$ core/shell NPs with a very thin SiO$_2$ shell of 2 nm placed at the CH$_3$NH$_3$PbI$_3$/TiO$_2$ interface yield poorer performance than that of the control device (Fig. S4 and Table S4, ESI†). For Au/SiO$_2$ core/shell NPs with relatively thicker shells (6 nm and 10 nm) placed at the CH$_3$NH$_3$PbI$_3$/TiO$_2$ interface, slightly improved device performances were observed although the relatively thicker SiO$_2$ shells could minimize carrier recombination on the Au core (Fig. S4 and Table S4, ESI†). Such performance improvement can be credited to the LSPR-induced enhancement of light absorption and promotion of carrier transport and collection.[28]

We now turn our attention to investigate the dielectric SiO$_2$ shell thickness-dependent charge carrier dynamics in PSCs

where plasmonic NPs are sandwiched within a TiO$_2$ ETL (scenario 1; Fig. 3a). Unless otherwise specified, the PSCs discussed below are assembled using CH$_3$NH$_3$PbI$_3$ as the absorber in a planar device configuration (denoted p-PSCs). In contrast to scenario 2, direct contact between the plasmonic Au and perovskite absorber is effectively prevented in scenario 1. As a result, the detrimental recombination pathway can be prohibited, and accordingly the charge carrier extraction efficiency in the PSC is improved. Fig. 3a depicts the device configuration of a planar PSC. A cross-sectional scanning electron microscopy (SEM) image is shown in Fig. 3b. Fig. 3c compares representative current density–voltage (J–V) curves of devices constructed using a pristine TiO$_2$ ETL (control device) and a double-layer TiO$_2$ ETL sandwiched with Au NPs and Au/SiO$_2$ core/shell NPs of different SiO$_2$ shell thicknesses. The detailed statistics of the parameters is summarized in Table S5 (ESI†). It was found that all devices based on plain Au NPs and Au/SiO$_2$ core/shell NPs with varied SiO$_2$ shell thickness show improved performance. A scrutiny of the J–V curves and parameter statistics reveals a shell-dependent device performance. First, for devices based on Au/SiO$_2$ NPs with relatively thick SiO$_2$ shell (6 nm and 10 nm), the enhanced PCE is primarily determined by the J_{sc}, whereas the V_{oc} and fill factor (FF) remain nearly constant. In sharp contrast, for devices constructed using plain Au NPs and Au/SiO$_2$ NPs with a very thin SiO$_2$ shell (2 nm), both J_{sc} and V_{oc} are markedly increased when compared to the control device (*i.e.*, in the absence of incorporation of plasmonic NPs within the TiO$_2$ ETL). Such an observation suggests the notably different underlying mechanisms responsible for the performance enhancement of the PSCs for these devices. The V_{oc} improvement induced by the introduction of plain Au NPs and Au/SiO$_2$ NPs of a 2 nm SiO$_2$ shell thickness is likely associated with the HET effect that may change the surface

1746 | *Energy Environ. Sci.*, 2020, **13**, 1743–1752

This journal is © The Royal Society of Chemistry 2020

potential of the TiO$_2$ ETL, thus decreasing the energy barrier for carrier transport from a perovskite photoactive layer to the TiO$_2$ ETL and increasing the built-in potential.[19,29] The increased V_{oc} was not observed for the Au core capped with a relatively thicker SiO$_2$ shell (6 nm and 10 nm). For Au/SiO$_2$ core/shell NPs, the hot electrons that reach the Au/SiO$_2$ interface can effectively overcome the electron tunneling barrier of the insulating SiO$_2$ at the SiO$_2$ thickness of $\leq$3 nm according to the literature.[23] Thus, for the 6 nm and 10 nm SiO$_2$ shells in present study, it is highly unlikely that the hot electrons from the Au core could transfer to the conduction band (CB) of TiO$_2$, suggesting that the HET effect does not play a role in this particular case. In addition, relatively thicker SiO$_2$ shells exhibit a suppression in the enhancement of J_{sc} due primarily to the restrained interaction between the localized electromagnetic field originated from Au and the carriers. Therefore, a thinner insulating SiO$_2$ shell of <3 nm is highly desirable for not only enabling a strong coupling of Au/SiO$_2$ NPs with the surrounding TiO$_2$ NPs, but also allowing hot carrier transfer over the SiO$_2$ tunneling barrier. As a result, devices based on both plain Au NPs and Au/SiO$_2$ NPs with a 2 nm thick SiO$_2$ shell yield better performance, especially for the plain Au NP-based device, achieving an optimal average PCE of 17.30% (Table S5, ESI†). Fig. S5 (ESI†) show the statistical results of device characteristics by varying the loading level of Au NPs sandwiched between a double-layer TiO$_2$ ETL in the p-PSCs. The optimal concentration of Au NP toluene solution was found to be 3 mg ml^{-1}. At this concentration, both the average J_{sc} and V_{oc} of the Au NP-based PSCs were improved, resulting in an absolute improvement of PCE. It is also important to note that there is no significant discrepancy between the reverse and forward device parameters (Fig. S6, ESI†), indicating less hysteresis and higher reliability of the J–V characteristics. Steady-state output PCE and photocurrent density of the control device and the device based on Au NPs sandwiched between a double-layer TiO$_2$ are shown in Fig. S7 (ESI†). Clearly, the Au NP-incorporated device delivers a stable output J_{sc} of 20.2 mA cm^{-2} and a PCE of 16.5%. While for the control device, the output J_{sc} and PCE are reduced to 18.30 mA cm^{-2} and 14.3%, respectively, indicating that the introduction of plain Au NPs in the TiO$_2$ ETL renders a stable device with a higher output energy under standard sunlight. Fig. S8 (ESI†) summarizes the statistical distributions of J_{sc}, V_{oc}, FF and PCE of a control device and Au NP-incorporated device. The average trend of the parameters is consistent with that of the representative devices shown in Fig. 3c (i.e., control device and Au NPs-incorporated device) and Table S5 (ESI†). It is clear that the most probable J_{sc} of 21.5 mA cm^{-2} and V_{oc} of 1.06 V are achieved from the Au NP-incorporated device, which are higher than those of the control device (J_{sc} = 20.0 mA cm^{-2} and V_{oc} = 1.03 V). Notably, by further optimizing the perovskite layer using a mixed FA$_{0.85}$MA$_{0.15}$PbI$_{2.55}$Br$_{0.45}$, the PCE of the resulting device that incorporates sandwiched Au NPs within the TiO$_2$ ETL is further improved from 17.22% (control device without Au NPs introduced into TiO$_2$ ETL) to 18.81% (Fig. 3d). The judicious sandwiching of Au NPs between a double-layer TiO$_2$ effectively circumvents the direct contact between Au NPs and the perovskite absorber, representing a critical step toward achieving high-performance devices. It is noteworthy that the assembly scenario 1 (Table S5, ESI†) yields higher device efficiencies over those from the assembly scenario 2 (Table S4, ESI†).

Scrutiny of mechanisms and charge carrier dynamics

In order to explore the mechanism that underpins the performance enhancement of PSCs based on a Au NP-incorporated TiO$_2$ ETL, incident photo-to-electron conversion efficiency (IPCE) measurements were first performed to evaluate the increased J_{sc} of the device (Fig. 4a). It is clear that the IPCE is improved via the introduction of Au NPs, yet the enhancement is broadly distributed over the entire spectral range and does not specifically follow the plasmonic absorption of Au NPs. It is noteworthy that both the maximal IPCE (Fig. 4a) and IPCE enhancement (Fig. S9, ESI†) were found to be around 525 nm, matching with the absorption peak of Au NPs and thus likely provides some evidence that the NEF enhancement of Au NPs indeed induces a PCE improvement of PSCs. The UV-vis absorption spectra of the perovskite layer deposited on the TiO$_2$ ETL with and without incorporation of Au NPs are shown in Fig. 4b. A very marginal improvement was seen for the Au NP-incorporated sample in the range of specific absorption wavelengths associated with Au NPs. We also found that there is no obvious morphology difference between perovskite films deposited on the double-layer TiO$_2$ ETL with and without the embedding of Au NPs (Fig. S2d and e, ESI†). The domain size and surface coverage are similar in the two films with high uniformity, which ensures a good light harvesting capability. Taken together, the incorporation of the as-prepared Au NPs in PSCs exerts a minor influence on the absorption and morphology. The simulation results show that the LSPR effect leads to a substantially non-uniform electric field distribution, which depends heavily on the wavelength of the incident light (Fig. S10, ESI†). However, this wavelength-dependent difference was not obviously observed in the UV-vis absorption measurement (Fig. 4b). This may be attributed to the large light absorption coefficient of perovskite as well as the low loading of Au NPs, suggesting that the J_{sc} enhancement cannot be attributed to the optical effect of plasmonic Au NPs. In contrast, the electronic characteristic of Au NPs plays a key role in increasing V_{oc} and J_{sc} and thus enhancing the performance of p-PSCs, as discussed below.

Subsequently, to compare the charge carrier dynamics, we performed time-integrated and time-resolved photoluminescence (PL) measurements on a perovskite-coated double-layer TiO$_2$ ETL with and without Au NPs sandwiched within the TiO$_2$ ETL. It is notable that spiro-OMeTAD is not present in these films. The time-integrated PL spectrum exhibits a significant reduction in the PL for the Au NP-incorporated sample (Fig. 4b). The time-resolved PL spectra at the perovskite emission peak of 778 nm are shown in Fig. 4c. A faster PL quenching was seen in the Au NP-incorporated sample. The bi-exponential fits yield the lifetime τ_1 of 39.46 ns and τ_2 of 135.31 ns for the control sample (i.e., no Au NPs sandwiched) and shorter τ_1 of 16.36 ns and τ_2 of 63.42 ns for the Au NP-incorporated sample. The accelerated PL quenching in the latter suggests a facilitated charge transfer from the perovskite to TiO$_2$.
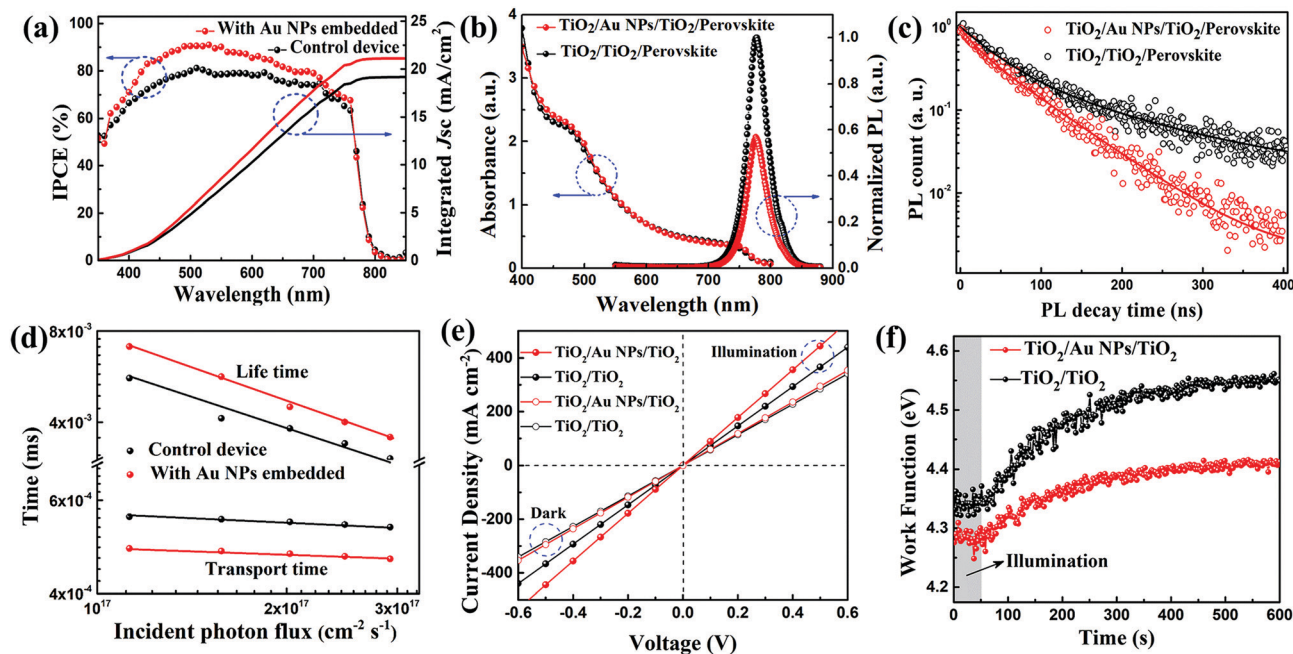
Fig. 4 (a) IPCE spectra, (b) UV-vis absorption and time-integrated PL spectra, (c) time-resolved PL spectra, (d) charge transit time and carrier lifetime, (e) J–V curves of conductivity test under illumination and dark conditions, and (f) work function changes after illumination measured by the Kelvin probe force microscope.

To further scrutinize the charge carrier dynamics in the device induced by the incorporated Au NPs, we conducted intensity modulated photocurrent spectroscopy (IMPS) and intensity modulated photovoltage spectroscopy (IMVS) measurements as a function of the incident light intensity (Fig. S11, ESI†). Both IMPS and IMVS measurements provide insight into the carrier lifetime and charge recombination dynamics, which have been widely used in DSSCs to determine the carrier lifetime (τ_n by IMVS) and charge transit time (τ_d by IMPS). A decreased τ_d and increased τ_n indicate the improved charge transport and carrier collection efficiency.[30–33] Fig. 4d compares the τ_d and τ_n for the devices with and without sandwiching Au NPs in the TiO$_2$ ETL. Clearly, the τ_d of the Au NP-incorporated device is shorter than that of the control device at varied incident photon flux, signifying a faster charge transport. The carrier lifetime τ_n reflects the recombination process in p-PSCs. The Au NP-incorporated device displays a longer τ_n compared to the control device. To further uncover the effect of plasmonic NPs on the carrier diffusion, we also calculated the diffusion coefficient of carriers D_n from τ_d and τ_n (Fig. S12, ESI†). Obviously, D_n of the Au NP-incorporated device is increased in comparison to that of the control device. Taken together, the introduction of plasmonic Au NPs favors the charge transport, the exciton dissociation, and the carrier mobility (as discussed below), which is consistent with previous work.[34]

To gain more physical insight into the electrical characteristic of p-PSCs, electrochemical impedance spectroscopy (EIS) was carried out under working conditions. Fig. S13a and b (ESI†) show the Nyquist plots of the devices measured at varied forward biases from 0 to 0.8 V. The high-frequency semicircle is attributed primarily to the contact resistance, and the main semicircle in the low frequency region represents the recombination resistance R_{rec} of charge carriers.[35] An equivalent circuit model (Fig. S13c, ESI†) was used to fit the Nyquist plots, from which R_{rec} at various applied biases can be obtained (Fig. S13d, ESI†). Clearly, at a fixed bias potential, the R_{rec} of the Au NP-incorporated device is much larger than that of the control device (no Au NPs sandwiched between a double-layer TiO$_2$), suggesting a markedly improved charge transfer for the Au NP-incorporated device. This observation accounts for the improved J_{sc} obtained from the J–V measurements. The EIS results correlated well with the IMPS and IMVS measurements discussed above. The prolonged lifetime τ_n and reduced transit time τ_d obtained from IMVS and IMPS studies, respectively, are originated from the improved charge transport within the ETL and the facilitated charge transfer and separation at the ETL/perovskite interface.

We note that the promoted charge separation and transport has been reported and ascribed to the reduced exciton binding energy induced by the NEF enhancement of the perovskite film with the incorporation of plasmonic Au/SiO$_2$ NPs (~ 8 nm SiO$_2$ shell) in the mesoporous alumina layer.[20] A reduced exciton binding energy could render charge separation in the photo-active perovskite or at the interfaces. However, in the present study with plain Au NPs or Au/SiO$_2$ NPs with a very thin shell (2 nm SiO$_2$), the additional possible reason that should be considered is the HET effect. The ability of Au NPs to create plasmonically excited electrons and impart charge transfer has been reported.[19,36] The accumulated energy induced by the LSPR on plain Au NPs or Au/SiO$_2$ NPs with an ultrathin shell can effectively dissipate in the form of either re-emitted photons or generated hot electrons.[19,34] A part of these hot electrons can transfer to the conduction band (CB) of neighboring TiO$_2$ and

1748 | Energy Environ. Sci., 2020, 13, 1743–1752

This journal is © The Royal Society of Chemistry 2020

even the perovskite absorber, thereby facilitating the carrier transport within the devices.[19,34,36,37] The surface plasmonically excited hot electron flow has been observed in the metal/semiconductor composites.[38] When it comes to the p-PSCs, the most possible dissipation pathway of hot electrons on the Au surface is for them to further interact with TiO_2, thus promoting local electron mobility in the TiO_2 ETL and ultimately leading to improved charge collection.[34,36] Consequently, the probability of charge transfer at the TiO_2 ETL/perovskite interface and charge transport within the TiO_2 ETL can be largely promoted.

To confirm the increased local electron mobility in the TiO_2 ETL induced by the HET effect due to the presence of Au NPs, a structure of FTO/double-layer TiO_2 (presence or absence of Au NPs)/Ag (Fig. S14, ESI†) was constructed. A similar device structure for the study of function layers in PSCs has been reported in the literature.[39,40] We simplified the mobility measurement by testing the conductivity difference under the dark and illumination conditions. As illustrated in Fig. 4e, under the dark conditions, the Au NP-incorporated TiO_2 film shows a slightly increased conductivity compared to the pristine TiO_2 film. In stark contrast, under illumination, the conductivity of both films is enhanced and the Au NP-incorporated TiO_2 film displays much higher photoconductivity, which favorably impacts the device performance under working conditions. We note that the excited hot electrons from Au NPs can transfer to TiO_2 (i.e., HET effect) and fill up the trap states of TiO_2, leading to increased charge carrier density and consequently improved conductivity of TiO_2.[21,34,36] On the other hand, the increased carrier density in TiO_2 induced by the HET effect increases the Fermi level of TiO_2 and lowers the work function of TiO_2

(Fig. 4f), resulting in enhanced built-in potential[19,37] and thus V_{oc}. To estimate the built-in potential of the devices, the Mott–Schottky analysis was performed at a frequency of 10 kHz with the bias potentials ranging from 0 to 1.2 V.[41,42] From the x-intercept of the linear regime in the Mott–Schottky plots (Fig. S15, ESI†), the built-in potentials of the control device and the Au NP-incorporated device were found to be 0.91 V and 0.94 V, respectively. The increased V_{oc} of the Au NP-incorporated device is in line with the enhanced built-in potential and the up-shift of the Fermi level. Compared to the control device with an average V_{oc} of 1.03 V, it increases to 1.06 V for the Au NP-incorporated device (Table S5, ESI†). The devices assembled using Au/SiO_2 NPs with a 2 nm SiO_2 shell show the same trend where the average V_{oc} increases to 1.05 V (Table S5, ESI†). Clearly, the increased V_{oc} is attributed to enhanced built-in potential and decreased energy barrier for carrier transport.

In this context, we propose that the HET from Au NPs to TiO_2 in conjunction with the promoted carrier transfer from perovskite to TiO_2 and charge transport within TiO_2 induced by the NEF enhancement accounts for the improved device performance. The trap states in TiO_2 form an extraction barrier between the photoactive layer and TiO_2, resulting in unfavorable electron extraction. It has been reported that UV-generated electrons in TiO_2 can fill up the trap states and thus enhance the conductivity.[21] The HET process is depicted in Fig. 5a and b. Upon excitation, hot electrons are generated in Au NPs. The excited hot electrons overcome the Schottky barrier (ϕ_B) between Au NPs and TiO_2 and are injected into the surrounding TiO_2 to passivate the trap states of TiO_2.

In the present study, capping the Au core with a SiO_2 shell of different thickness provides a convenient route to assessing the
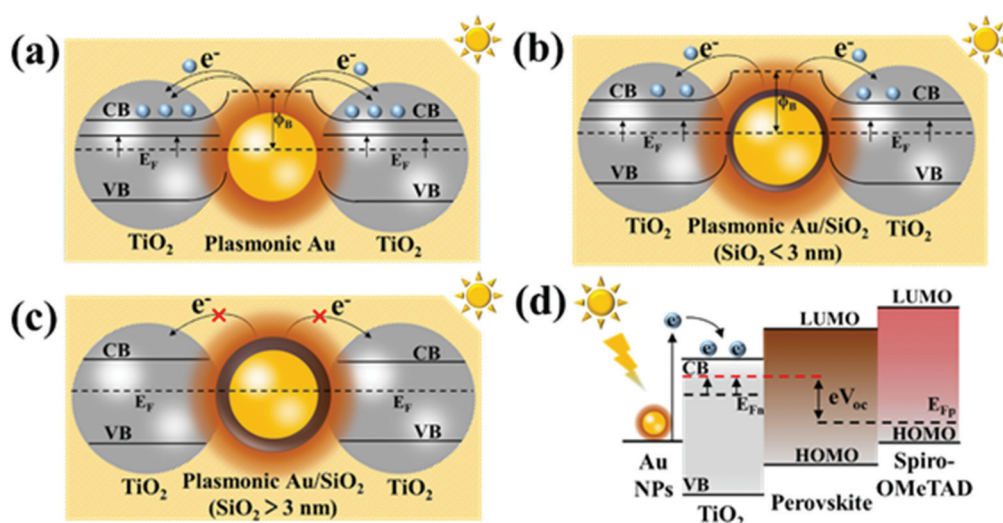
Fig. 5 Schematic illustration of LSPR-induced HET and NEF enhancement for plasmonic NPs (Au NP and Au/SiO_2 core/shell NP) sandwiched between a double-layer TiO_2 ETL. (a) TiO_2/Au NP/TiO_2, (b) TiO_2/(Au/SiO_2 NP)/TiO_2 (SiO_2 < 3 nm), and (c) TiO_2/(Au/SiO_2 NP)/TiO_2 (SiO_2 > 3 nm). (d) Schematic diagram of the mechanism of the HET process for the trap-filling and the corresponding increased built-in potential of the device due to the up-shift of the Fermi level of TiO_2. It is notable that the LSPR effect is seen in (a)–(c), and an up-shift in Fermi level as a result of the HET process from the Au NPs to TiO_2 is seen in only (a) and (b). The brown halo in (a)–(c) represents the NEF enhancement. CB and VB are the conduction band and valence band, respectively. ϕ_B in (a) and (b) is the Schottky barrier height between Au and TiO_2. E_F in (a)–(c) is the apparent Fermi level. E_{Fn} and E_{Fp} in (d) are the Fermi level of electrons and holes, respectively. The red dashed line in (d) depicts the increased Fermi level due to the HET effect.

This journal is © The Royal Society of Chemistry 2020

Energy Environ. Sci., 2020, **13**, 1743–1752 | **1749**

role of plasmonic NPs in PSCs. When Au/SiO_2 NPs with a relatively thick shell are employed, their influence is limited primarily to the NEF enhancement-induced promotion of carrier transfer from perovskite to TiO_2 and charge transport within TiO_2 (Fig. 5c). It is important to note that such effect does not alter the apparent Fermi level of the double-layer TiO_2 film. If plain Au or Au/SiO_2 NPs of a very thin SiO_2 shell are in contact with TiO_2, they are capable of transferring hot electrons to the neighboring TiO_2 and undergoing the Fermi level equilibration.[19,37] The Fermi level up-shift results in a longer electron lifetime and a higher recombination resistance, ultimately leading to improved charge transport and increased V_{oc} (Fig. 5d). Notably, earlier reports on plasmonic PSCs have demonstrated a clear increase in V_{oc} of approximately 10–30 mV by exploiting Ag/TiO_2[43] and Au NPs.[44]

Effectiveness of the TiO_2/Au NPs/TiO_2 ETL in mesostructured PSCs

In addition to the planar PSCs discussed above, to demonstrate the effectiveness of the TiO_2/Au NPs/TiO_2 ETL in tailoring charge carrier dynamics of PSCs, we also capitalized on the sandwich-like ETL for mesostructured PSCs (denoted m-PSCs) by adding an additional mesoporous TiO_2 layer on the sandwiched TiO_2/Au NPs/TiO_2 film (Fig. 6a and b). Fig. 6c and Fig. S16 (ESI†) present the statistics of photovoltaic characteristics of m-PSCs based on the $FA_{0.85}MA_{0.15}PbI_{2.55}Br_{0.45}$ absorber assembled with the TiO_2/Au NPs/TiO_2 and TiO_2/TiO_2 (i.e., control sample) ETLs. The most probable J_{sc} of 22.3 mA cm^{-2} and V_{oc} of 1.07 V are achieved from the device based on TiO_2/Au NPs/TiO_2 ETL, which are much higher than those of the control device (J_{sc} = 20.9 mA cm^{-2} and V_{oc} = 1.04 V) (Fig. S16a and b, ESI†).

Fig. 6 (a) Device configuration and (b) cross sectional SEM image of mesostructured PSC (denoted m-PSC) assembled using $FA_{0.85}MA_{0.15}$-$PbI_{2.55}Br_{0.45}$ as an absorber and TiO_2/Au NPs/TiO_2 as the ETL. (c) The statistics of PCEs for 30 m-PSCs assembled using $FA_{0.85}MA_{0.15}PbI_{2.55}Br_{0.45}$ as an absorber with and without Au NPs sandwiched between double-layer TiO_2 as the ETL, respectively. (d) J–V characteristics of the champion m-PSCs assembled using $FA_{0.85}MA_{0.15}PbI_{2.55}Br_{0.45}$ as an absorber with (PCE = 19.42%) and without (PCE = 17.76%) Au NPs sandwiched between double-layer TiO_2 as the ETL, respectively.

It is worth noting that the optimal m-PSC constructed by using $FA_{0.85}MA_{0.15}PbI_{2.55}Br_{0.45}$ as an absorber and TiO_2/Au NPs/TiO_2 as the ETL delivers a markedly enhanced PCE of 19.42%, compared to that of the optimal control device (PCE = 17.76%) (Fig. 6d).

Device stability

Due to effective charge trap passivation of TiO_2 via HET from Au NPs, the issues associated with interfacial reaction and the ion migration in PSCs can be alleviated, thereby improving the device stability.[45] Both p-PSCs and m-PSCs with and without Au NPs sandwiched between a double-layer TiO_2 were stored in a desiccator without encapsulation and evaluated under ambient conditions (temperature: 25 ± 2 °C, relative humidity: 30 ± 5%) (Fig. S17, ESI†). For control devices (no Au NPs incorporated), they only retain 68.8% and 57.6% of their original PCEs after one-month for p-PSCs and m-PSCs, respectively. In stark contrast, the devices with introduced Au NPs manifest an improved durability, experiencing only 14.5% and 17.8% PCE loss for p-PSCs and m-PSCs, respectively.

Conclusions

In summary, we developed an understanding on how judicious design of plasmonic NPs of different dimensions and architectures as well as their interfacial positioning facilitates the tailoring of charge carrier dynamics in PSCs. Such investigation is enabled by the use of amphiphilic star-like block copolymer nanoreactors to craft monodisperse plain Au and Au/SiO_2 core/shell NPs with a fixed Au core diameter and varied SiO_2 shell thickness. The presence of the SiO_2 shell exerts a profound influence on the J_{sc} and V_{oc} of PSCs. When sandwiching Au/SiO_2 core/shell NPs within a TiO_2 ETL, the resulting PSCs containing Au/SiO_2 core/shell NPs with 6 nm and 10 nm thick SiO_2 shells produce only higher J_{sc} compared to the control device constructed in the absence of Au or Au/SiO_2 NPs sandwiched between a double-layer TiO_2 ETL. In stark contrast, both plain Au NPs and Au/SiO_2 NPs with a very thin SiO_2 shell of 2 nm experience the HET that passivates the trap states in TiO_2, leading to improved charge transfer from perovskite to TiO_2 and transport within the TiO_2 ETL and thus increased J_{sc}. Moreover, the HET process also leads to increased carrier density in TiO_2 that shifts the Fermi level of TiO_2 upward, resulting in increased V_{oc}. Taken together, both J_{sc} and V_{oc} for plain Au NPs and Au/SiO_2 NPs with the SiO_2 shell thickness t_{SiO_2} of 2 nm are much larger than those of the abovementioned cases (i.e., t_{SiO_2} of 6 nm and 10 nm). Consequently, the optimal planar and mesostructured PSCs engineered using the TiO_2/Au NPs/TiO_2 ETL (i.e., plain Au NPs sandwiched between a double-layer TiO_2) yield the champion PCEs of 18.81% and 19.42%, respectively (scenario 1). Notably, the devices fabricated by impregnating Au NPs via scenario 1 outperform those by placing plasmonic NPs at the perovskite/TiO_2 interface (scenario 2). This study offers insight into the tailoring of charge carrier dynamics in PSCs via rational design and placement of monodisperse plasmonic/dielectric NPs with tunable dielectric shell
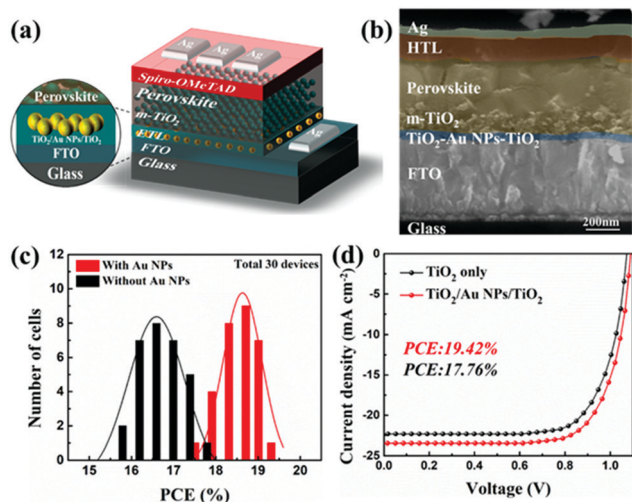
1750 | *Energy Environ. Sci.*, 2020, **13**, 1743–1752

This journal is © The Royal Society of Chemistry 2020

thickness to achieve plasmonic enhancement-enabled high-performance PSCs. Moreover, as precursors amenable to the star-like block copolymer nanoreactor strategy are virtually unlimited, conceptually a myriad of functional NPs with accurately controlled sizes, architectures, and composition can be readily created for use in solar-to-chemical energy conversion, controlled nano-scale light–matter interaction, *etc.*

Conflicts of interest

There are no conflicts to declare.

Acknowledgements

Notes and references

1 NREL's ''Best Research-Cell Efficiencies'' Chart, https://www.nrel.gov/pv/cell-efficiency.html.

2 M. He, D. Zheng, M. Wang, C. Lin and Z. Lin, *J. Mater. Chem. A*, 2014, **2**, 5994–6003.

3 X. Liu, Y. Wang, X. Cui, M. Zhang, B. Wang, M. Rager, Z. Shu, Y. Yang, Z. Li and Z. Lin, *J. Mater. Chem. A*, 2019, **7**, 165–171.

4 A. Kojima, K. Teshima, Y. Shirai and T. Miyasaka, *J. Am. Chem. Soc.*, 2009, **131**, 6050–6051.

5 W. Chen, Y. Wu, Y. Yue, J. Liu, W. Zhang, X. Yang, H. Chen, E. Bi, I. Ashraful and M. Grätzel, *Science*, 2015, **350**, 944–948.

6 W. S. Yang, B.-W. Park, E. H. Jung, N. J. Jeon, Y. C. Kim, D. U. Lee, S. S. Shin, J. Seo, E. K. Kim and J. H. Noh, *Science*, 2017, **356**, 1376–1379.

7 B. Wang, J. Iocozzia, M. Zhang, M. Ye, S. Yan, H. Jin, S. Wang, Z. Zou and Z. Lin, *Chem. Soc. Rev.*, 2019, **48**, 4854–4891.

8 M. He, B. Li, X. Cui, B. Jiang, Y. He, Y. Chen, D. O'Neil, P. Szymanski, M. A. Ei-Sayed, J. Huang and Z. Lin, *Nat. Commun.*, 2017, **8**, 16045.

9 M. Yang, T. Zhang, P. Schulz, Z. Li, G. Li, D. H. Kim, N. Guo, J. J. Berry, K. Zhu and Y. Zhao, *Nat. Commun.*, 2016, **7**, 12305.

10 D. P. McMeekin, G. Sadoughi, W. Rehman, G. E. Eperon, M. Saliba, M. T. Hörantner, A. Haghighirad, N. Sakai, L. Korte and B. Rech, *Science*, 2016, **351**, 151–155.

11 Q. Chen, H. Zhou, T.-B. Song, S. Luo, Z. Hong, H.-S. Duan, L. Dou, Y. Liu and Y. Yang, *Nano Lett.*, 2014, **14**, 4158–4163.

12 M. Ye, C. He, J. Iocozzia, X. Liu, X. Cui, X. Meng, M. Rager, X. Hong, X. Liu and Z. Lin, *J. Phys. D: Appl. Phys.*, 2017, **50**, 373002.

13 H. Zhou, Q. Chen, G. Li, S. Luo, T.-B. Song, H.-S. Duan, Z. Hong, J. You, Y. Liu and Y. Yang, *Science*, 2014, **345**, 542–546.

14 M. D. Brown, T. Suteewong, R. S. S. Kumar, V. D'Innocenzo, A. Petrozza, M. M. Lee, U. Wiesner and H. J. Snaith, *Nano Lett.*, 2010, **11**, 438–445.

15 J. Qi, X. Dang, P. T. Hammond and A. M. Belcher, *ACS Nano*, 2011, **5**, 7108–7116.

16 X. Liu, J. Iocozzia, Y. Wang, X. Cui, Y. Chen, S. Zhao, Z. Li and Z. Lin, *Energy Environ. Sci.*, 2017, **10**, 402–434.

17 K. Awazu, M. Fujimaki, C. Rockstuhl, J. Tominaga, H. Murakami, Y. Ohki, N. Yoshida and T. Watanabe, *J. Am. Chem. Soc.*, 2008, **130**, 1676–1680.

18 N. Aeineh, E. M. Barea, A. Behjat, N. Sharifi and I. Mora-Sero, *ACS Appl. Mater. Interfaces*, 2017, **9**, 13181–13187.

19 Z. Yuan, Z. Wu, S. Bai, Z. Xia, W. Xu, T. Song, H. Wu, L. Xu, J. Si and Y. Jin, *Adv. Energy Mater.*, 2015, **5**, 1500038.

20 W. Zhang, M. Saliba, S. D. Stranks, Y. Sun, X. Shi, U. Wiesner and H. J. Snaith, *Nano Lett.*, 2013, **13**, 4505–4510.

21 C. S. Kim, S. S. Lee, E. D. Gomez, J. B. Kim and Y.-L. Loo, *Appl. Phys. Lett.*, 2009, **94**, 84.

22 A. O. Govorov, H. Zhang and Y. K. Gun'ko, *J. Phys. Chem. C*, 2013, **117**, 16616–16631.

23 W. R. Erwin, A. Coppola, H. F. Zarick, P. Arora, K. J. Miller and R. Bardhan, *Nanoscale*, 2014, **6**, 12626–12634.

24 Y. J. Yoon, Y. Chang, S. Zhang, M. Zhang, S. Pan, Y. He, C. H. Lin, S. Yu, Y. Chen, Z. Wang, Y. Ding, J. Jung, N. Thadhani, V. V. Tsukruk, Z. Kang and Z. Lin, *Adv. Mater.*, 2019, **31**, e1901602.

25 X. Li, J. Iocozzia, Y. Chen, S. Zhao, X. Cui, W. Wang, H. Yu, S. Lin and Z. Lin, *Angew. Chem., Int. Ed.*, 2018, **57**, 2046–2070.

26 X. Pang, L. Zhao, W. Han, X. Xin and Z. Lin, *Nat. Nanotechnol.*, 2013, **8**, 426–431.

27 K. Matyjaszewski and N. V. Tsarevsky, *Nat. Chem.*, 2009, **1**, 276–288.

28 K. Chan, M. Wright, N. Elumalai, A. Uddin and S. Pillai, *Adv. Opt. Mater.*, 2017, **5**, 1600698.

29 A. Guerrero, S. Chambon, L. Hirsch and G. Garcia-Belmonte, *Adv. Funct. Mater.*, 2014, **24**, 6234–6240.

30 J. H. Heo, D. H. Song, H. J. Han, S. Y. Kim, J. H. Kim, D. Kim, H. W. Shin, T. K. Ahn, C. Wolf and T. W. Lee, *Adv. Mater.*, 2015, **27**, 3424–3430.

31 J. H. Heo, H. J. Han, D. Kim, T. K. Ahn and S. H. Im, *Energy Environ. Sci.*, 2015, **8**, 1602–1608.

32 M. Cha, P. Da, J. Wang, W. Wang, Z. Chen, F. Xiu, G. Zheng and Z.-S. Wang, *J. Am. Chem. Soc.*, 2016, **138**, 8581–8587.

33 X. Meng, X. Cui, M. Rager, S. Zhang, Z. Wang, J. Yu, Y. W. Harn, Z. Kang, B. K. Wagner, Y. Liu, C. Yu, J. Qiu and Z. Lin, *Nano Energy*, 2018, **52**, 123–133.

34 R. Fan, L. Wang, Y. Chen, G. Zheng, L. Li, Z. Li and H. Zhou, *J. Mater. Chem. A*, 2017, **5**, 12034–12042.

35 M. He, X. Pang, X. Liu, B. Jiang, Y. He, H. Snaith and Z. Lin, *Angew. Chem., Int. Ed.*, 2016, **55**, 4280–4284.

36 W. R. Erwin, H. F. Zarick, E. M. Talbert and R. Bardhan, *Energy Environ. Sci.*, 2016, **9**, 1577–1601.

37 D. Zhang, W. C. Choy, F. Xie, W. E. Sha, X. Li, B. Ding, K. Zhang, F. Huang and Y. Cao, *Adv. Funct. Mater.*, 2013, **23**, 4255–4261.

38 Y. K. Lee, C. H. Jung, J. Park, H. Seo, G. A. Somorjai and J. Y. Park, *Nano Lett.*, 2011, **11**, 4251–4255.

This journal is © The Royal Society of Chemistry 2020

Energy Environ. Sci., 2020, **13**, 1743–1752 | 1751

39 R. O'Hayre, M. Nanu, J. Schoonman and A. Goossens, *J. Phys. Chem. C*, 2007, **111**, 4809–4814.

40 S. van Reenen, M. Kemerink and H. J. Snaith, *J. Phys. Chem. Lett.*, 2015, **6**, 3808–3814.

41 A. Guerrero, E. J. Juarez-Perez, J. Bisquert, I. Mora-Sero and G. Garcia-Belmonte, *Appl. Phys. Lett.*, 2014, **105**, 133902.

42 T. Bu, J. Li, F. Zheng, W. Chen, X. Wen, Z. Ku, Y. Peng, J. Zhong, Y. B. Cheng and F. Huang, *Nat. Commun.*, 2018, **9**, 4609.

43 M. Saliba, W. Zhang, V. M. Burlakov, S. D. Stranks, Y. Sun, J. M. Ball, M. B. Johnston, A. Goriely, U. Wiesner and H. J. Snaith, *Adv. Funct. Mater.*, 2015, **25**, 5038–5046.

44 S. S. Mali, C. S. Shim, H. Kim, P. S. Patil and C. K. Hong, *Nanoscale*, 2016, **8**, 2664–2677.

45 H. Dong, T. Lei, F. Yuan, J. Xu, Y. Niu, B. Jiao, Z. Zhang, D. Ding, X. Hou and Z. Wu, *Org. Electron.*, 2018, **60**, 1–8.